Delft University of Technology

Thermal, optical and mechanical properties of new glass compositions containing fly ash

Justino de Lima, C.L.; Veer, F.A.; Zhang, H.; França de Mendonça Filho, F.; Copuroglu, Oguzhan; Nijsse, R.

Important note
To cite this publication, please use the final published version (if applicable).
Please check the document version above.

Thermal, optical and mechanical properties of new glass compositions containing fly ash

Clarissa Justino de Lima,[a,b,1] *Fred Veer,*[c] *Hongzhi Zhang,*[a] *Fernando França de Mendonça Filho,*[a]
Oguzhan Copuroglu[a] *& Rob Nijsse*[a,c]

[a] *Department of materials, mechanics, management & design (3Md), Delft University of Technology, the Netherlands*
[b] *American Glass Research, the Netherlands*
[c] *Department of Architectural Engineering & Technology, Delft University of Technology, the Netherlands*

The investigation of new compositions is crucial for the expansion of possible applications of glass, from the typical applications for building engineering, in the form of cast blocks or float glass, to more advanced technologies, such as 3D-printed glass or glass-to-metal connections. Since high melting temperatures and brittleness are two important drawbacks of glass, this work aims to improve both properties. Characterisation techniques, such as thermal analysis, nano-indentation, and UV/VIS spectroscopy, are used to evaluate the properties of the samples. The modification of the properties is achieved via changes in the composition of the glass, using compounds such as phosphorus pentoxide, aluminium oxide and boron oxide. Then, the choice of different glass formers and modifiers contributes to the development of compositions with lower melting and glass transition temperatures. The reduction of the melting temperature allows a saving of energy during the manufacturing. The structures of the glasses differ from the standard soda–lime–silica and borosilicate glasses, leading to a different mechanical behaviour. Furthermore, these new compositions incorporate up to 35% of fly ash in their formulas. The valorisation of these by-products reduces costs and gas emission.

1. Introduction

The utilisation of industrial waste in manufacturing building materials has increased considerably due to concerns over the amount of waste produced and the significant environmental problems caused by its disposal. Expanding populations, urbanisation, and increased wealth are ramping up the global production of solid waste. Factors like population and per capita gross domestic product (GDP) are used to measure total global municipal solid waste (MSW) production.[1] The waste production rates per capita usually grow with wealth, despite the fact that there is a tendency toward anti-materialism in wealthier countries. When combined, these aspects indicate a scenario in which, over the next decades, global waste generation will go beyond our capacity to control it.[1]

Fly ash is a by-product from burning pulverised coal in electric power generating plants, it can be used in Portland cement concrete (PCC) pavement, paving roads, regular structural concrete, or any other normal concrete, among others. Even with the shift from the energy generation modes from thermal to other renewable sources, the dependence on coal is expected to be significant in the next decades. This culminates in a large amount of fly ash generation

and the ways that need to be explored for its better utilisation.

Coal-fired power plants are declining as a result of the growing popularity of renewable energy and cleaner forms of fuel, such as natural gas. As a by-product of the coal combustion process, the fly ash generation is directed by the consumption of coal for electricity generation. The percentage of electric power from coal is predicted to decrease from 39% of total generation in 2013 to 34% in 2033.[2] However, the combination of economic growth and an increasing population will drive increasing demand for electricity. Consequently, coal electric generation is projected to grow by 3·4% from 2013 to 2033, according to the US Energy Information Association.[2] According to a survey by the American Coal Ash Association (ACAA), approximately 37 million tons of fly ash were produced in the US in 2018.[3] Of this, around 20 million tons were used in concrete and other applications. The rest was disposed of in landfills.

Many countries still did not reach an optimal utilisation of fly-ash. For instance, in India and China, the top two countries based on annual fly ash generation, the current percentage utilisation is quite behind the target. As per a 2018 report by the Central Electricity Authority (CEA), about 57% of the total power generated in India is produced by coal-based

power plants. Globally, coal provides around 27% of overall energy supplies and generates about 38% of the world's electricity. This percentage is expected to remain stable for the next 30 years.[4]. Even with numerous initiatives, taken at the policy level by various ministries and a large number of technological developments by the various R&D organisations for gainful utilisation, the percent of fly ash utilisation in India was 67·13% in 2018. From this amount of fly ash, approximately 38·67% is utilised in the construction sector for various modes, like 25·60% in cement, 9·01% in bricks and tiles, 3·40% in roads and flyovers, and 0·66% in concrete.[5] In China, the percent of fly ash utilisation was 70% in 2016.[5]

As a considerable amount of coal combustion products (CCPs) is still sent to disposal, pollution control agencies and environmental groups are putting increased pressure on power producers to find more valuable uses for ash. A conservative estimation of the quantity of CCPs in disposal across the US exceeds 2 billion tons.[6] Technologies under development can provide new opportunities to use CCPs, and part of this volume, disposed in landfills and ponds, will be reclaimed for beneficial use. Even with the long list of applications for fly ash utilisation, no individual application can assure 100% use of fly ash. For this reason, a reasonable mix of applications is unavoidable. Cement and concrete have reached the threshold limit and will not accommodate more than 35–40% of overall ash generated in the next years.[5] Therefore, it is understood that the cement and concrete alone would not be able to utilise the total production of fly ash and new alternatives have to be found and promoted.

Despite a significant number of products developed from fly ash, most of them consist of non-transparent materials, partly because it is a challenge to get transparent materials in reasonable temperatures from this by-product. Fly ash contains many elements that are also present in typical glass formulas. For instance, the elements found in higher amounts in the chemical systems of standard silicate glasses are SiO_2, Na_2O, CaO, K_2O, MgO and Al_2O_3.[7] All these elements are found in fly ash compositions. Some of these components are highly refractory and their presence in complex compositions means they are highly likely to crystallise and have high working temperatures. However, glass is a material that allows large amounts of various elements in solution, being suitable to assimilate complex compounds in its compositions. Therefore, this work aimed at characterising new glass recipes, which incorporate up to 35% of fly ash in their compositions, while keeping transparency and relatively low working temperatures.

The choice of the element used as the glass former is the first step in designing a glass composition. Phosphate glasses possess relatively low working temperatures, low liquidus viscosity, large ultra-violet transparency, and high solubility for other glass modifiers or intermediaries.[8] For this reason, phosphate was used as a glass former in this work.

The compound KPO_3 was chosen as the phosphate source. Like other alkali metal ions, potassium can be incorporated between the chains, each formed from PO_4 tetrahedron. Alkali metal ions have a small electric field intensity and a small electronegativity. Consequently, the bonding strength between the alkali metal ion and an oxygen ion is small, while linear chains formed from PO_4 tetrahedra can be connected to each other by weak bonding strength through alkali metal ions.[9] The effect of these weak bonds is reflected in the low melting temperature of the glass; however, it also has poor chemical durability.

Since binary alkali phosphate glasses have poor chemical durability, it is necessary to add additional elements into the formula of the glass, namely polyvalent element oxides. Cations of polyvalent elements can inhibit the penetration of water into a glass structure by increasing the bonding strength between the chains of a metaphosphate glass. Among the polyvalent element oxides, there are divalent elements, which can improve water resistance to a certain extent, as they have a relatively small electric field intensity and electronegativity and have a relatively small bonding strength compared to an oxygen ion. Among these oxides, there is MgO and CaO, present in fly ash. Other oxides, such as Al_2O_3 and Fe_2O_3, are also present in fly ash (Table 1). These oxides contain cations that form a crosslinking structure between those and a phosphorous ion through an oxygen ion.[9] They are able to improve the water resistance more than the divalent elements. Fly ash proved to be a great and inexpensive source of polyvalent element oxides.

The first attempts at melting aimed to obtain samples from a mixture of KPO_3 and fly ash, however produced non-transparent materials. The addition of aluminium oxide (Al_2O_3) yielded transparent glass samples. Diboron trioxide (B_2O_3) was added to some samples in an attempt to decrease the thermal expansion coefficient of the glasses.

The developed samples already had their structures analysed by x-ray diffraction (XRD), which confirmed the amorphous character of the samples with the highest amounts of fly ash.[10] Some samples had their compositions verified using x-ray fluorescence (XRF); the results are shown in Table 2. The concentration of B_2O_3 could not be determined as boron cannot be measured by XRF. Thus, the concentration of this element was predicted based on the concentrations

Table 1. Composition of fly ash (FA) determined by x-ray fluorescence

	SiO_2	Al_2O_3	CaO	MgO	Fe_2O_3	SO_3	Na_2O	K_2O	TiO_2	P_2O_5	LOI
FA	54·28	23·32	4·23	1·62	8·01	0·64	0·85	1·97	1·23	0·54	3·37

Table 2. Compositions of the glass samples containing fly ash, expressed in wt% and mol%

Sample concentration:	70KPO$_3$–15FA–15Al$_2$O$_3$		60KPO$_3$–20FA–20Al$_2$O$_3$		40KPO$_3$–25FA–15Al$_2$O$_3$–20B$_2$O$_3$	
	wt%	mol%	wt%	mol%	wt%	mol%
SiO$_2$	8·36	14·97	10·31	17·47	13·86	21·17
B$_2$O$_3$	-	-	-	-	14·32	18·88
Al$_2$O$_3$	19·55	20·62	24·44	24·40	21·75	19·57
Na$_2$O	-	-	-	-	0·18	0·26
K$_2$O	27·96	31·92	25·47	27·53	18·54	18·06
MgO	0·24	0·65	0·29	0·72	0·38	0·86
CaO	0·69	1·33	0·78	1·42	1·15	1·89
SrO	0·02	0·02	0·03	0·02	0·04	0·03
BaO	0·28	0·19			0·10	0·06
ZrO$_2$	0·01	0·01	0·18	0·15	0·11	0·08
ZnO	0·09	0·12	0·11	0·14	0·01	0·01
TiO$_2$	0·17	0·23	0·23	0·30	0·34	0·39
Cr$_2$O$_3$	-	-	-	-	0·01	0·01
MnO	0·01	0·02	0·01	0·02	0·02	0·02
SO$_3$	0·02	0·02	0·02	0·02	0·01	0·01
Fe$_2$O$_3$	1·26	0·85	1·64	1·05	2·51	1·44
P$_2$O$_5$	38·29	29·01	37·22	26·69	26·64	17·22
CuO	-	-	-	0·01	0·01	0·01
GeO$_2$	-	-	0·03	0·03	-	-
Rb$_2$O	-	-	-	-	0·01	-
I	-	-	0·02	0·02	-	-
NiO	0·01	0·01	0·01	0·01	0·01	0·02
O/P molar ratio	-	4·73	-	5·16	-	7·85

of the other elements. The homogeneity of the glasses was confirmed by compositional maps obtained with energy dispersive spectroscopy (EDS).

The water resistance of the samples was improved with changes in the compositions, achieving high water resistance. A high water resistance was reported for the samples containing an amount equal or lower than 70 wt% of KPO$_3$. There is a trend of increasing elastic modulus and hardness of the samples with amounts of fly ash and Al$_2$O$_3$. These properties were measured according to a continuous stiffness measurement. All these results were already reported, as well as the preparation of the samples.[10]

The current work aims to report the characteristic temperatures, optical properties, coefficient of thermal expansion (CTE), and mechanical properties of the samples. The results would be useful to compare the properties of these glasses to standard glasses used for building purposes and to suggest potential applications for them.

2. Methods

Making the samples: the glasses were melted in a Carbolite high temperature box furnace, model HTF 17/10, which can operate up to 1700°C. The samples were prepared in a 30 mL platinum crucible and cooled under melt quenching. The melted mixtures were poured into a stainless steel mould preheated to around 450°C and were annealed at this temperature for 3 h before cooling to room temperature inside the furnace. This annealing schedule guarantees stress-free samples, as confirmed through cross-polarised light. For the nomination of the sample, KPO$_3$ represents the amount of KPO$_3$, FA represents the amount of fly ash and Al$_2$O$_3$ represents the amount of Al$_2$O$_3$, all in wt%. For instance, the sample 55KPO$_3$–35FA–

10Al$_2$O$_3$ contains 55% (wt) of KPO$_3$, 35% (wt) of fly ash and 10% (wt) of Al$_2$O$_3$.

X-ray fluorescence (XRF): was used to determine the actual composition of the samples. The investigated samples were flat, dimensions about 2·5×5 cm, and thickness of approximately 0·5 cm. The measurements were performed with a Panalytical Axios Max WD-XRF spectrometer and data evaluation was done with SuperQ5.0i/Omnian software.

X-ray powder diffraction (XRD): was used to prove the amorphous character of the samples. The samples were investigated as fine powder, homogeneised in a ceramic mortar. A thin layer of sample powder was deposited on a Si510 wafer from a powder-ethanol suspension and fixed in PMMA sample holder L510. The instrument used in the analysis was a Bruker D8 Advance diffractometer Bragg-Brentano geometry and Lynxeye position sensitive detector, using Cu Kα radiation.

Differential scanning calorimetry and thermogravimetry analysis (DSC-TGA): was used to obtain the characteristic temperatures of the samples. Differential scanning calorimetry and thermogravimetry were performed using a Netzsch STA F3 Jupiter, using a heating rate of 10 K/min.

UV/VIS spectroscopy: was used to determine the absorption of radiation of the samples as a function of wavelength. The UV/VIS spectroscopy was performed with a spectrophotometer Perkin-Elmer Lambda 950 UV-VIS-NIR.

Nanoindentation: the measures of fracture toughness were conducted with a KLA-Tencor G200 nano-indenter using Berkovich and Knoop tips. The prepared glass samples had their surfaces polished, and then the samples were reannealed.

Microscopy: microscopic images were obtained with an environmental scanning electron microscope

(ESEM) Philips XL30 ESEM and an optical polarisation and fluorescence microscope.

Thermal expansion tests: was applied to measure the coefficient of thermal expansion of the glasses. The gauges type ZFLA-6-11 attached to the samples were connected to wires of a DAQ device of three channels. The device was also connected to a computer. The samples were placed inside a Heraeus oven type UT 12P, which is operational up to 250°C. The test ranged from 30–163°C. A bridge-compensation circuit was used outside the oven while inside it used a quarter bridge sensing gauge.

3. Results and discussions

3.1. Characteristic temperatures

Through DSC curves, it was possible to determine the characteristic temperatures of the samples. Based on these characteristic temperatures, it was also possible to determine the parameter of thermal stability of the systems, as shown in Table 3. This was achieved by comparing the T_g and T_x obtained for each sample. The level of thermal stability against crystallisation marks the difference between the starting crystallisation temperature and the glass transition temperature (T_x–T_g). Both temperatures were determined on the DSC curves using the tangent method. It is assumed that the glass forming tendency is proportional to the thermal stability of glass. The glass forming tendency is expressed numerically, thus enabling one to compare different kinds of glasses and the influence of various impurities.[11] Besides the T_g, possible inflections were observed in the DSC curves of the samples containing the lowest amounts of fly ash, remarkably the sample containing 12·5% of fly ash. We recommend repeating the thermal analysis for these samples and further investigation about possible phase separation.

The DSC-curves of the samples containing from 12·5 to 35% of fly ash (Figure 1) show that higher concentrations of fly ash and Al_2O_3 correlate with an increase in glass transition temperatures. In addition, thermal stability decreases with increasing concentrations of fly ash (Table 3). As the enthalpy of a transition is derived from the area under its curve, the sample with the lowest amount of KPO_3, shows the crystallisation peak with the highest enthalpy. This tendency to crystallise goes with the high con-
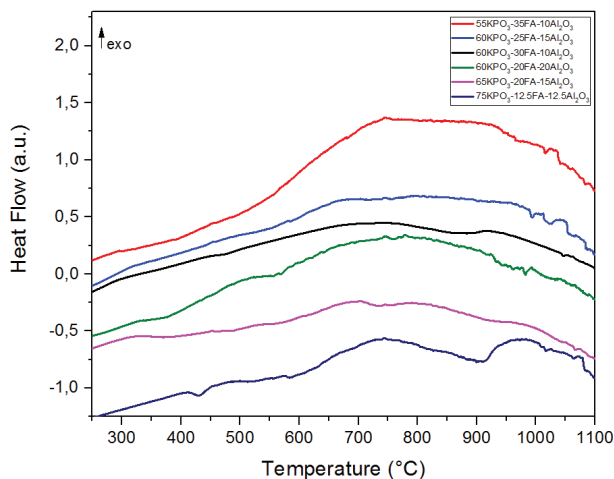

Figure 1. DSC curves of the glasses containing fly ash, in which the amount of fly ash ranges from 12·5–35% (wt) [Colour available online]

centrations of different oxides present in this sample, due to it containing the highest concentrations of fly ash and aluminium oxide.

Two samples were produced with the addition of B_2O_3: $50KPO_3$–$10B_2O_3$–25fly ash–$15Al_2O_3$ and $40KPO_3$–$20B_2O_3$–25fly ash–$15Al_2O_3$. There is a marginal decrease in T_g with the addition of B_2O_3: the glass transition temperature of the sample with 10% (wt) of B_2O_3 is around 475°C, while the sample containing 20% (wt) of the same oxide has a glass transition temperature of 472°C (Figure 2). A meaningful change introduced by increasing the amount of B_2O_3 is the crystallisation behaviour of the sample. While the sample with the lowest amount of this oxide presents two following crystallisation peaks, the first starting around 514°C and peaking around 650°C and the second one peaking around 860°C, the sample containing 20% of B_2O_3 presents only one peak, starting around 640°C and peaking around 810°C. Thus, the interval between the T_x and
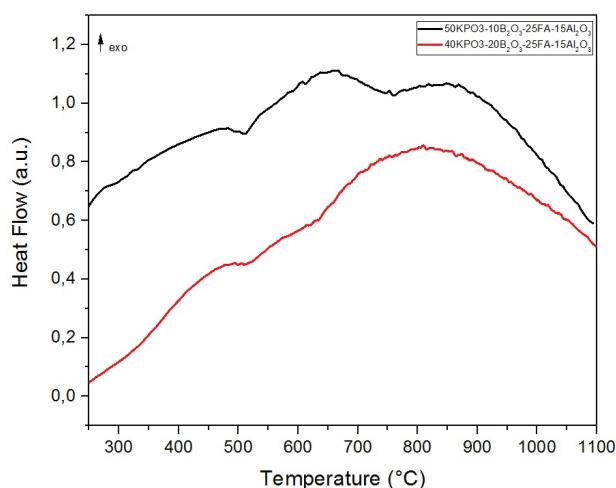
Table 3. Characteristic temperatures and thermal stability of glasses containing fly ash (FA)

Sample	T_g (°C)	T_x (°C)	T_x–T_g (°C)
$55KPO_3$–$35FA$–$10Al_2O_3$	456	510	54
$60KPO_3$–$25FA$–$15Al_2O_3$	458	535	77
$60KPO_3$–$30FA$–$10Al_2O_3$	460	530	70
$60KPO_3$–$20FA$–$20Al_2O_3$	484	564	80
$65KPO_3$–$20FA$–$15Al_2O_3$	451	569	118
$75KPO_3$–$12·5FA$–$12·5Al_2O_3$	412	602	190
$50KPO_3$–$10B_2O_3$–$25FA$–$15Al_2O_3$	475	514	39
$40KPO_3$–$20B_2O_3$–$25FA$–$15Al_2O_3$	472	640	168

Figure 2. DSC curves of the glasses containing fly ash and B_2O_3 [Colour available online]

T_g is significantly higher for the sample with the highest amount of this oxide, showing that increasing the amount of B_2O_3 produces samples with a higher thermal stability against devitrification.

3.2. Optical spectroscopy

The samples consisting of 35% fly ash showed a green coloration and were produced at 1350°C. The samples consisting of 15% fly ash were yellow and can be produced at lower temperatures, 1100°C. Higher concentrations of fly ash made samples become darker and also increased melting temperature.

The colours of some samples containing fly ash are summarised in Table 4 and their optical spectra are shown in Figure 3. The samples contain between 1·3 and 2·5% (wt) of Fe_2O_3. The states of transition metals in host glass, and thus the ratio of these two iron species, not only depends on composition but also on the redox conditions of the melt, such as air atmosphere, melting temperature and melting time.[12] It is known that alkali borate and alkali silicate glass types favour the presence of transition metal ions (i.e. iron) in higher oxidation states. On the other hand, alkali phosphate glasses induce a lower oxidation state.[13]

Fe^{2+} and Fe^{3+} are, respectively, blue and yellow chromophores. The CT bands of Fe^{2+} are located at higher energies and therefore lower wavelengths that those of Fe^{3+}. Ferric Fe^{3+} is mainly identified by an absorption band at 380 nm. Ferrous Fe^{2+} is characterised by a strong absorption band with a maximum of around 1050 nm, thus already outside the visible range. The broadness of the band may be indicative of the Jahn–Teller distortion of the octahedrally coordinated ion, an effect often found in octahedral complexes of transition metals. It is expected that the band of tetrahedrally coordinated Fe^{2+} ions would be found around 2000 nm in the near infrared.[14]

The ratio between Fe^{2+}/Fe^{3+} explains the colour of the glass types. While the two species can appear simultaneously in a sample, its ratio is affected by the composition of the glass and its melting conditions. The intensities of the band related to Fe^{3+} are quite similar for the three samples, but the intensity
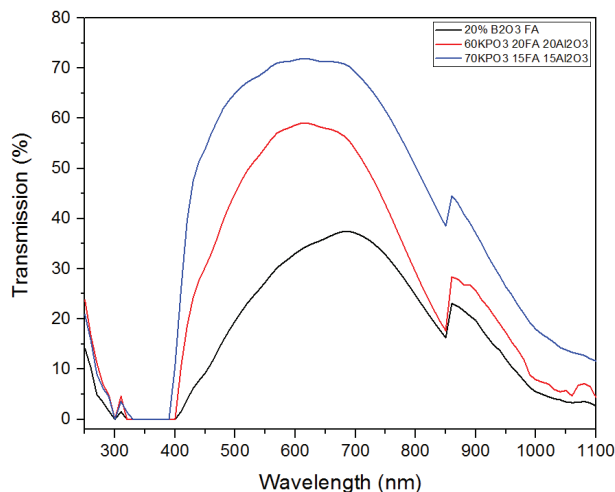

Figure 3. Optical spectra of samples containing fly ash [Colour available online]

of the absorption at 1050 nm is notably higher for the sample $40KPO_3–20B_2O_3–25FA–15Al_2O_3$, followed by the sample with 20% of fly ash and then 15% of fly ash. As the ratio Fe^{2+}/Fe^{3+} decreases, the colour of the glass changes from dark green (20% B_2O_3) to yellow (15% fly ash). Green-coloured glass could therefore be associated with a relative increase in the concentration of ferrous ions, while a yellow colour is associated with a lower value of Fe^{2+}/Fe^{3+}, thus a relative higher amount of ferric ion.

The spectra exhibit a step at 850 nm, which is related to a fall from the baseline due to the replacement of the detector, as the scan is made from infrared to visible and the sensitivity of the detectors at 850 nm is different. Theoretically, with careful correction of the baseline and extracting the blank sample, it is possible to extract this event. However, in practice, there is usually some effect left. Therefore, this step is not related to the properties of the samples.

3.3. Thermal expansion

Determining the thermal expansion coefficient of a glass is fundamental in order to predict the susceptibility to thermal shocks and the crack propagation after rapid cooling.

Table 4. Colours of different glasses containing fly ash as glass beads of 3 mm [Colour available online]

$40KPO_3–20B_2O_3–25FA–15Al_2O_3$	$60KPO_3–20FA–20Al_2O_3$	$70KPO_3–15FA–15Al_2O_3$
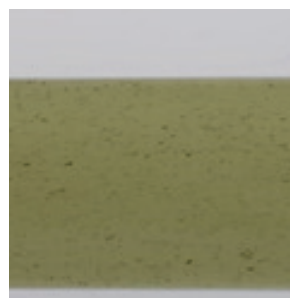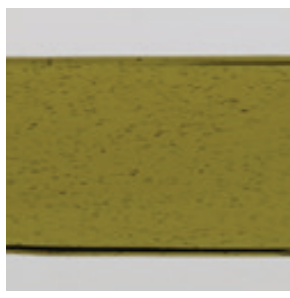
Table 5. CTE obtained for different glasses

Sample	$\alpha \times 10^{-6}/°C$
$40KPO_3–20B_2O_3–25FA–15Al_2O_3$	5.7 ± 0.2
$50KPO_3–10B_2O_3–25FA–15Al_2O_3$	6.2 ± 0.7
Flat glass (Kimble R-6)	9.0 ± 0.2
$60KPO_3–30FA–10Al_2O_3$	10.4 ± 0.3
Borosilicate (B270 from Schott)	7.6 ± 0.9
$70KPO_3–15FA–15Al_2O_3$	14.1 ± 0.8

Table 5 shows the values of the coefficient of thermal expansion (CTE) measured by strain gauges for glasses containing fly ash in relation to two commercial glasses. The commercial tested glasses were a borosilicate crown glass (B270 from Schott) and a soda–lime–silica float glass (Kimble R-6).

Samples without B_2O_3 expand more than the other glasses. The CTE increases with the increasing amount of KPO_3, thus with higher amounts of K_2O and P_2O_5. The samples with 60% of KPO_3 have a CTE slightly above the one of soda–lime glasses. However, the glasses containing 70% of KPO_3 have a CTE much higher than borosilicate or soda–lime glasses, which limit their applications in architectural engineering as they will be sensitive to temperature shocks.

An increasing CTE when alkalis are added to phosphate glasses is probably caused by the depolymerisation of anions. On the other hand, additions of Al_2O_3 and fly ash could increase the degree of polymerisation. Linear relations were already found between the expansion coefficient and the radius of alkali cations for a series of compositions in the systems $R_2O–Al_2O_3–P_2O_5$:[15] the expansion increases with increasing radius. This trend suggests that the increase in expansion is a result of the decrease in the strength of the cationic field and the expansion would mainly be determined by the interaction between cations and nonbridging oxygens.

The high water resistance of the developed samples containing fly ash was already reported and showed that the water resistance increases with decreasing amounts of KPO_3.[15] This is consistent with studies reporting an increase in expansion coefficient together with the increase of the dissolution rate of a phosphate glass, indicating that both properties are controlled primarily by the interaction of cations with nonbridging oxygens.[15] High expansion glasses with good chemical durability are desirable for applications such as bonding with plastics or metals, since the thermal expansion coefficient of the joining materials should be proximate. However, high values of CTE mean sensitivity to thermal shock which limits the applications of phosphate glasses in other areas, such as building materials. The development of new glass compositions, containing lower amounts of phosphate and higher amounts of fly ash or B_2O_3 demonstrated to decrease the CTE of the glasses, producing samples with a coefficient of expansion comparable to the coefficient of soda–lime and borosilicate glasses, or even lower. It expands the range

of applications of typical phosphate glasses, showing potential uses in construction, such as bricks, or even in more advanced technologies which require a combination of low melting temperatures and low thermal expansion, such as 3D printing.

3.4. Mechanical properties

Nanoindentation has been extensively applied as a high spatial resolution micro-probe for measuring the mechanical properties of glasses at the micro-level. The mechanical properties that can be measured by this technique include: hardness, elastic modulus, and fracture toughness.[16] A crucial factor in the expansion of the use of nanoindentation is the simple sample preparation. A small glass sample requires only grinding and polishing, achieving a surface free of scratches. In addition, most indentation equipment offers experimental control of test parameters, which is necessary for the exploration of different deformation modes by changing experimental time scale, indenter tip geometry, and loading conditions.[15]

Traditional testing methods for fracture toughness determination are generally based on macroscopic crack extension experiments. However, evaluating the fracture toughness of glasses and ceramics is still problematic. Consequently, a mechanism for measuring fracture toughness of these materials has not been well determined. The nanoindentation test is an option that has been used in order to assess the fracture toughness of brittle materials; such as glasses, ceramics, films, and coatings. Where the materials exhibit brittle fracture with minimal crack tip plasticity, this crack pattern can be used to establish fracture toughness values.[18] This property can be estimated by either crack length-based method or crack energy-based method, providing useful partially quantitative information. The tests were performed under 2 N and with a distance of 200 μm between the indents. As some samples did not crack under these conditions, new tests were performed with a Knoop indenter under a load of 8.5 N.

Although somewhat problematic, fracture toughness evaluation can be quickly performed using indentation. If a sharp tip is forced into a bulk sample of a brittle material, radial cracking usually occurs after a critical load has been reached, originating from stress concentrations at the diamond facet edges, which allows an estimate of the fracture toughness based on the maximum indentation load and the crack length.[19] In indentation-based methods with sharp pyramidal indenters, the fracture toughness can be determined from measurements of the lengths of cracks emerging from the residual indentation impression.[16] An equation proposed by Evans[20] and Lawn[21] allows the calculation of K_c based on indentation tests, measuring the length of cracks originating from the edges of the indent impression,
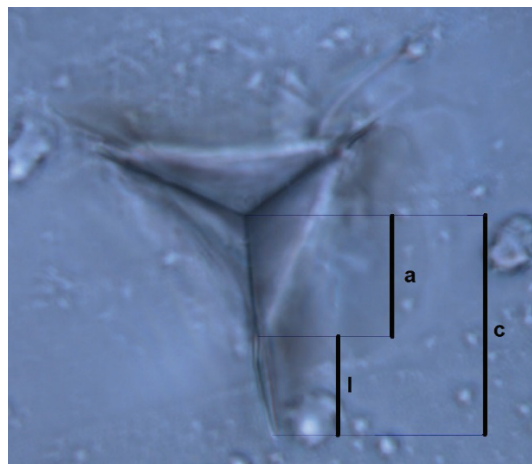
Figure 4. Dimensions of a crack induced by a Berkovich indenter, in which c=a+l [Colour available online]

determining that:

$$K_c = A \left(\frac{E}{H} \right)^{1/2} \frac{P}{c^{3/2}} \qquad (1)$$

In which E=Young's modulus, H=hardness, P=load, c=crack length measured from the centre of the indent to the crack tip. A is an empirical constant, which varies according to the indenter and the crack geometry.[19] For a Berkovich indenter, A=0·016.[22] The representative dimensions of the pyramidal indentation fracture testing method are shown in Figure 4.

A crack is classified as well developed if $c \gg a$. However, if the radial cracks are not well developed, the relation between K_C and $P/c^{3/2}$ ceases.[23] The method presented above can be applied only to well-developed radial cracks. Some authors reported that the linear relation between K_{IC} and $P/c^{3/2}$ stops when $c<2·5a$.[24,25] Other authors claimed that the relation is valid even when c is down to $1·1a$.[26,27] The different glass compositions were analysed by optical microscopy and presented huge variations in crack lengths. At least five indents were made in each sample. In many cases, the images obtained with the use of microscopy can be related to the load–displacement curves. For instance, the sample $40KPO_3$–$20B_2O_3$–$25FA$–$15Al_2O_3$, in which the microscopy does not reveal the presence of cracks, and the load–displacement curve does not show any significant pop-in (Figure 5). The sample $60KPO_3$–$20FA$–$20Al_2O_3$ shows well-developed cracks, which can be related to the pop-ins of high energy, present in the load–displacement curve (Figure 6).

For the fracture toughness estimation based on the length of the cracks, only defined cracks, with $c/a>1·1$, were considered. For bulk brittle materials, this method provides a calculation within 40% accuracy.[28] The most significant source of error is probably the unknown crack geometry. The models make presumptions about crack geometry, the half-penny type or Palmquist, and this assumption influences
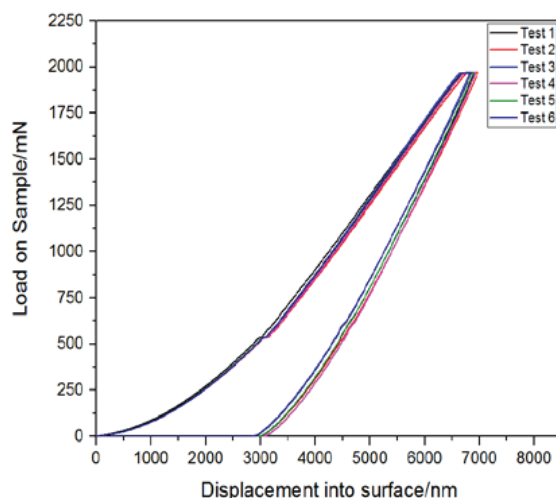

Figure 5. Microscopic image and load–displacement curve of the sample $40KPO_3$–$20B_2O_3$–$25FA$–$15Al_2O_3$ under 2 N, using a Berkovich indenter [Colour available online]

the crack area considered. If the real crack geometry is different than the assumed geometry, the model will yield erroneous conclusions.[29]

In the case of undeveloped cracks, an energy-based model was used, based on the load–displacement curve associated with the fracture. In this work, the shapes of the indentation load–displacement (P–h) curves reveal predominant elastic–plastic deformation, in which the hysteresis is caused mainly by plastic deformation mechanisms. It is opposed to the brittle behaviour, in which the indentation hysteresis is mostly generated by fracture.[17] The maximum displacement into the surface of the samples containing fly ash is significantly higher than the soda–lime sample (Figures 7 and 8). This agrees with the lower hardness values of these materials, which should allow a higher penetration depth under the same load.

Energy-based models can be used to deal with various cracking patterns. A largely applied energy-based model was proposed by Li,[30] consisting of extrapolating the loading curve where there is a fracture-induced pop-in. The P–δ curve is extrapo-
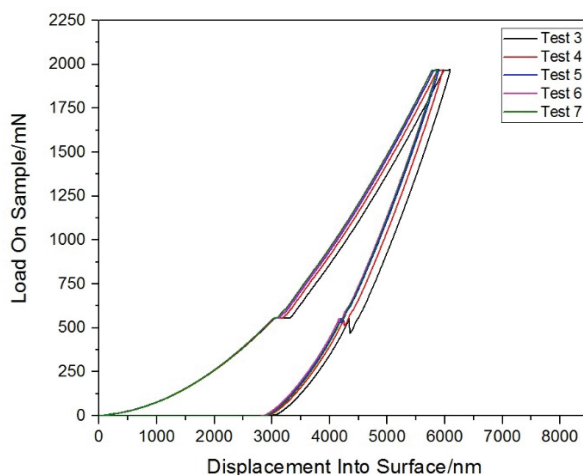
Figure 6. Microscopic image and load–displacement curve of the sample 60KPO$_3$–20FA–20Al$_2$O$_3$ under 2 N, using a Berkovich indenter [Colour available online]

lated from the start point (onset of the fracture) to its end point. The area under the load–displacement curve corresponds to the work performed by the indenter during the elastic–plastic deformation of the system.[30] The difference between the extrapolated curve and the measured curve is considered as the fracture dissipated energy.[23] This energy difference (*U*) was calculated for all the tests of every sample. Calculating fracture toughness by measuring fracture energy requires an estimate of the area *F* of the crack. For a Berkovich indenter, it can be adapted to:[29]

$$F = \frac{\pi c^2}{4} - \frac{a^2}{2} \qquad (2)$$

Estimating the fracture toughness can be done according to the following equation, which applies to any crack shape:[30]

$$K_c = \sqrt{\frac{E}{1-v^2}\frac{U}{F}} \qquad (3)$$

In which *E*=Young's modulus, *v*=Poisson ratio,

U=crack energy from pop-in and *F*=crack area. In this work, it was assumed that *v*=0·35 for phosphate glasses and *v*=0·25 for soda–lime glass. The calculated values of fracture toughness can be found in Table 6.

Due to the absence of developed cracks in most samples, new tests were performed using a higher load and another indenter geometry, the Knoop indenter. The cracks were analysed with optical microscopy and scanning electron microscopy. Figure 9 and Table 7 show the average dimensions of the indents produced for different samples.

The dimensions of the samples varied among the different compositions. Remarkably, the soda–lime sample has a low value of *L*, while the sample containing fly ash and 20% of B$_2$O$_3$ has a remarkably low *W*. Different patterns of cracks were associated to different glass compositions.

Some of the indents in soda–lime possess extended cracks on both sides with interference fringes, indicating the presence of lateral cracks.

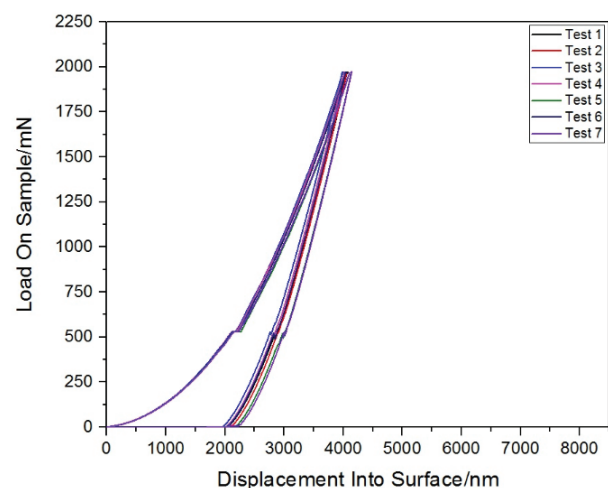The samples containing 30 and 35% fly ash present

Figure 7. Load–displacement curve of soda–lime–silica glass under 2 N, using a Berkovich indenter [Colour available online]
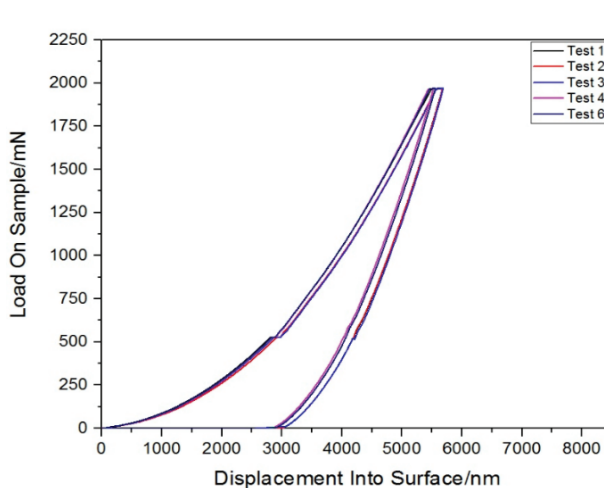

Figure 8. Load–displacement curve of the sample 55KPO$_3$–35FA–10Al$_2$O$_3$ under 2N, using a Berkovich indenter [Colour available online]

Table 6. K_c calculation based on the equations of Li (energy) and Lawn & Evans (crack lengths)

Sample	Average a (μm)	Average c (μm)	c/a	E (GPa)	H (GPa)	Kc (MPa√m) Li	Kc (MPa√m) Lawn & Evans
40KPO₃–20B₂O₃–25FA–15Al₂O₃	17·91	19·53	1·09	48·4	5·02	0·42	*
55KPO₃–35FA–10Al₂O₃	18·15	18·15	1·00	43·5	4·18	**	*
60KPO₃–20FA–20Al₂O₃	19·13	30·30	1·58	41·6	3·94	0·80	0·62
60KPO₃–30FA–10Al₂O₃	20·31	20·31	1·00	45·2	4·56	**	*
Soda–lime–silica (reference)	14·33	24·84	1·73	74·0	5·50	0·44	0·94

*As c/a<1·1 these K_c values are not reliable. **As $c=a$ there is no crack. Therefore, these K_c values are not reliable and reflect a pessimistic lower boundary.

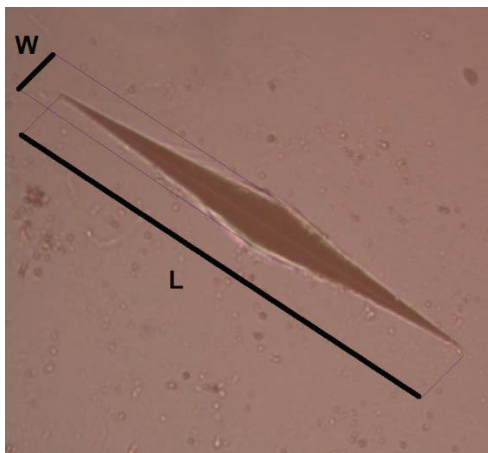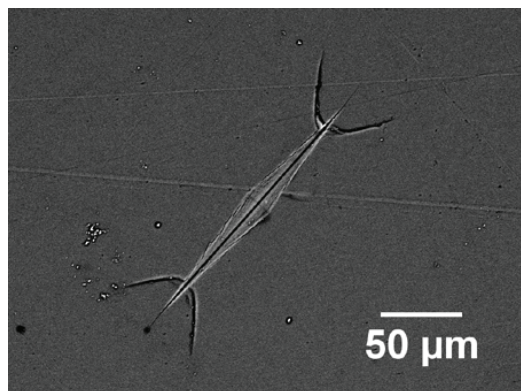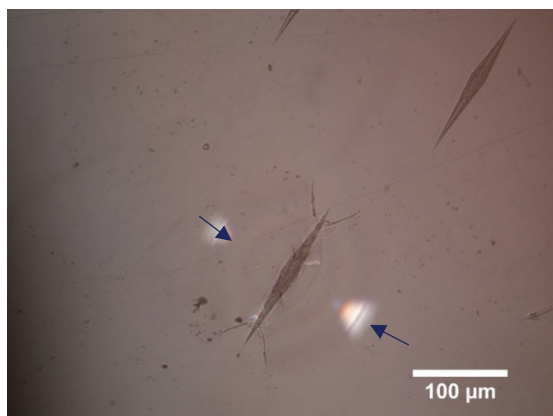*Figure 9. Dimensions of a Knoop indent [Colour available online]*

similar fracture patterns with edge cracks, as shown in Figures 11 and 12.

(a)

(b)

Figure 10. Crack pattern of a silicate glass induced by a load of 8·5 N using a Knoop indenter a) indent analysed by SEM b) interference fringes (blue arrows) [Colour available online]

Table 7. Average dimensions of the Knoop indent in the samples

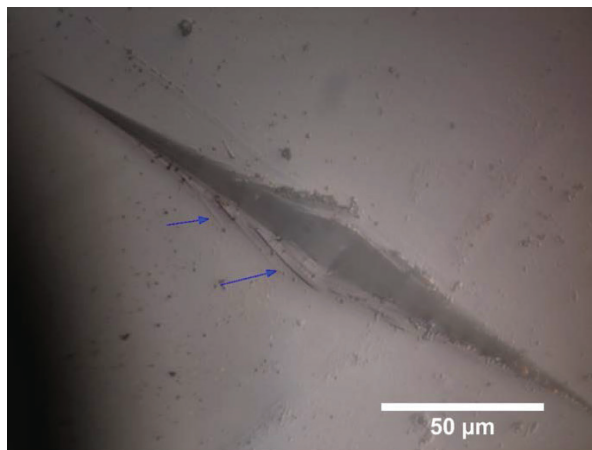| Sample	L (μm)	Std. Dev. (L)	W (μm)	Std. Dev. (W)
40KPO₃–20B₂O₃–25FA–15Al₂O₃	261·20	0·09	9·25	0·52
60KPO₃–30FA–10Al₂O₃	209·20	3·85	21·00	1·17
55KPO₃–35FA–10Al₂O₃	208·10	1·82	21·46	0·76
Soda–lime–silica (reference)	162·42	2·66	21·32	0·11

Figure 11. Crack pattern of 60KPO₃–30FA–10Al₂O₃ induced by a load of 8·5 N using a Knoop indenter. Arrows point to the edge cracks [Colour available online]

The sample containing fly ash and 20% of B₂O₃ has radial cracks and an indentation pattern of an arrow, in which the dimension W is kept almost constant for all the extension of the sample.
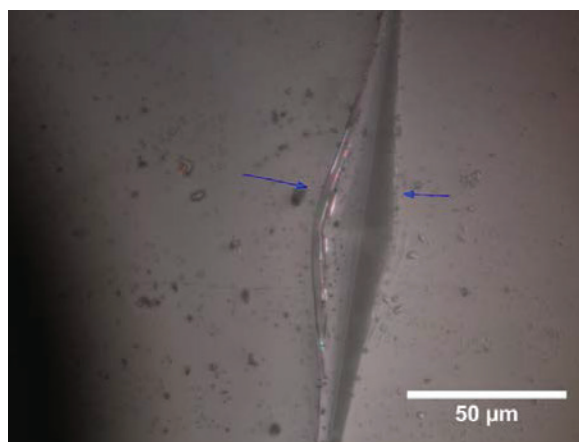
The indentation pattern detailed in Figure 13 dif-

Figure 12. Crack pattern of 55KPO₃–35FA–10Al₂O₃ induced by a load of 8·5 N using a Knoop indenter. Arrows point to the edge cracks [Colour available online]
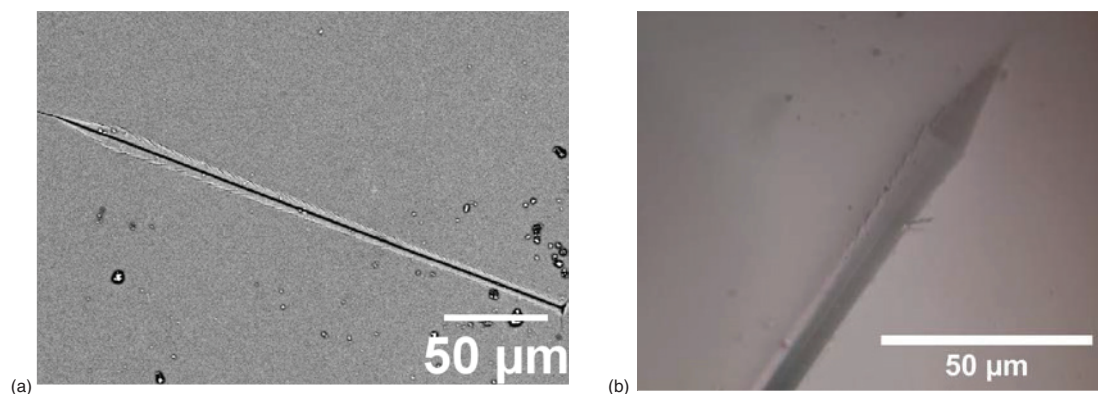
Figure 13. Crack pattern of the sample $40KPO_3$-$20B_2O_3$-$25FA$-$15Al_2O_3$ induced by a load of 8·5 N using a Knoop indenter (a) indent analysed by SEM (b) close-up of the cracks analysed by optical microscopy [Colour available online]

fers significantly from typical Knoop indents, and no reports of it were found in the literature.

Following this, new indentation tests were performed under the same conditions as the previous test, but in four different directions, as indicated in Figure 14. Three indents were performed in each direction. Different results were obtained for different directions. The DSC-curve presented in Figure 2, which has a defined glass transition temperature, combined with the x–ray diffraction pattern presented in Figure 15, which proves that it is a predominantly amorphous sample, indicates a possible anisotropic behaviour of the material.

While glasses are mostly isotropic materials, anisotropy is not incompatible with a lack of crystalline order. Anisotropy was already reported for some glasses, such as a metaphosphate glass of composition $12\cdot5Li_2O$–$12\cdot5Na_2O$–$12\cdot5K_2O$–$12\cdot5Cs_2O$–$50P_2O_5$ (mol%). In this case, the enhancement of the mechanical properties was attributed to the orientation of $-P-O-P-$ chains in the glass.[31] Alkali metaphosphate glasses, $50R_2O$–$50P_2O_5$ (mol%), in which R_2O
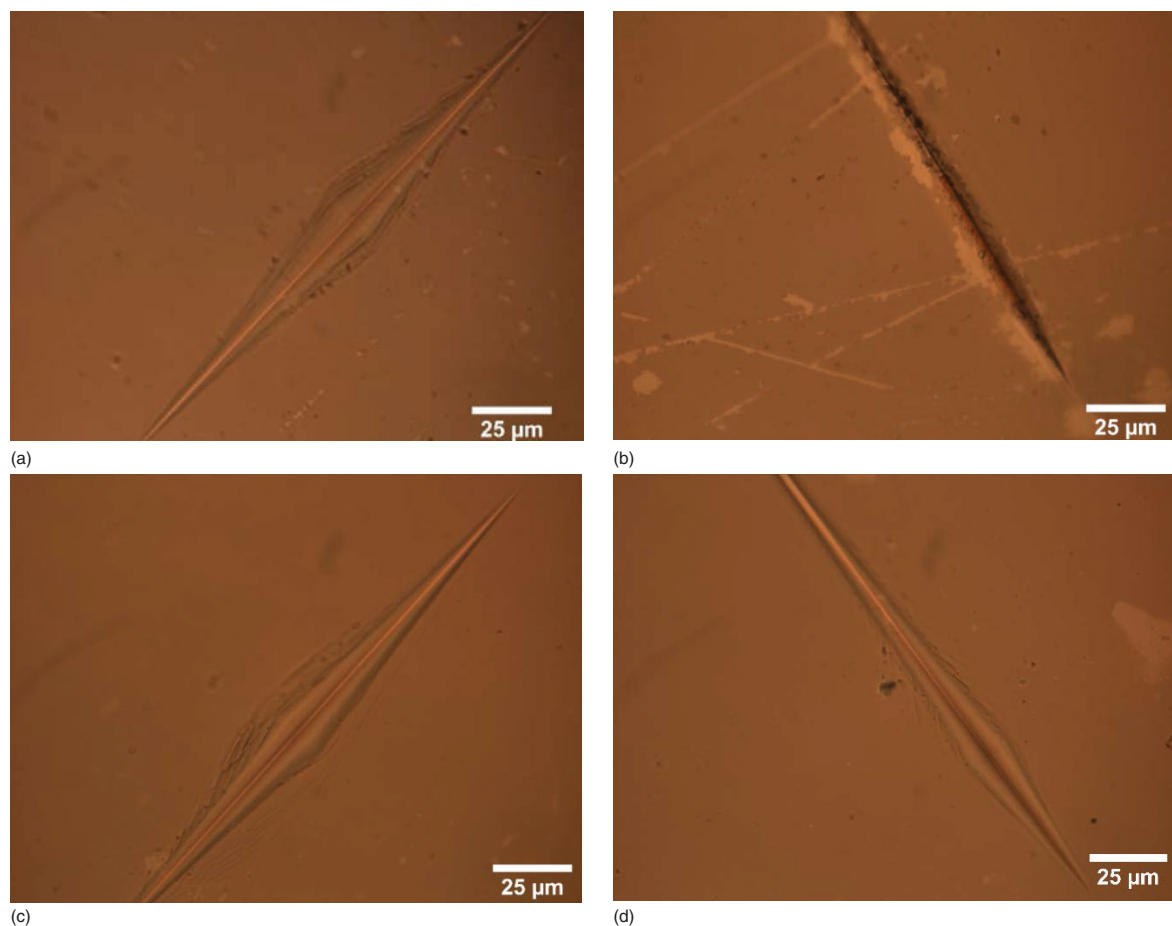
Figure 14. Close-up of crack patterns of the sample $40KPO_3$–$20B_2O_3$–$25fly ash$–$15Al_2O_3$ induced by a load of 8·5 N using a Knoop indenter and measured at every 90° (a), (b), (c), (d) [Colour available online]

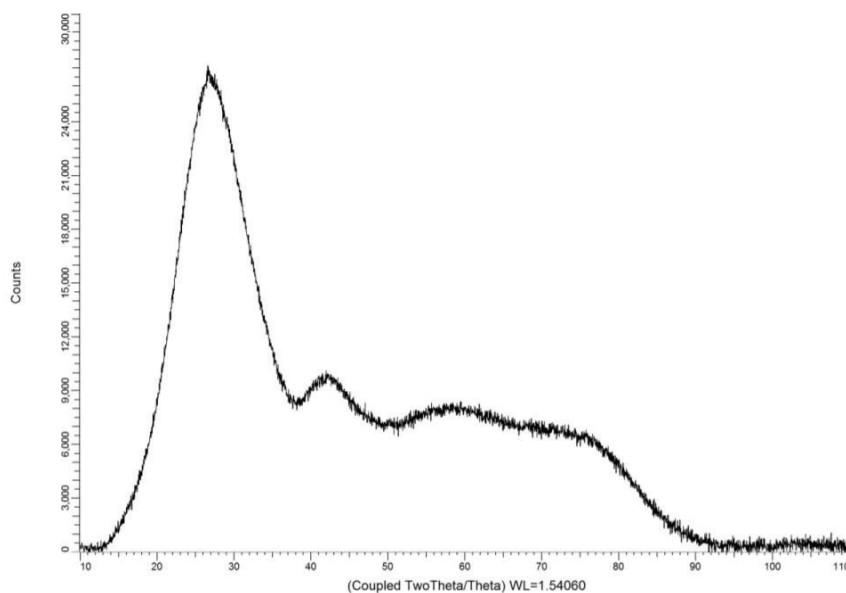*Figure 15. X-ray diffraction pattern of the sample 40KPO₃–25FA–15Al₂O₃–20B₂O₃*

represents an alkali oxide, possess a structure mainly formed by one-dimensional −P–O–P− chains because their PO_4 tetrahedral units are connected by two oxygen atoms (*n*=2). If these chains are randomly organised, the metaphosphate glasses will be isotropic. However, $NaPO_3$ and KPO_3 metaphosphate crystals are anisotropic. Both have uniaxially oriented P–O–P chains, $NaPO_3$ in a spiral orientation and KPO_3 in a zigzag manner. When the chains in glass are uniaxially organised, such as in metaphosphate crystals, anisotropic glasses can be formed.[31] Another work from the same authors reports the occurrence of entropic elasticity in phosphate glasses with highly anisotropic structures.[9] Oxide glasses generally possess three-dimensional networks, consisting of oxygen polyhedra surrounding network-forming cations, such as Si^{4+}, B^{3+} and P^{5+}. However, metasilicate and metaphosphate glasses are usually based on chain structures in which oxygen tetrahedra are connected by their two corners and the chains are composed of covalent bonds, with some degree of ionic character. Typical metaphosphate glasses have chains containing between 40 and 100 P-tetrahedra, ended by hydroxyl groups or modifiers, such as alkali ions.[9] The chains connect with each other by ionic bonding via modifiers. It is expected that oxide glasses with a rubberlike structure, containing highly polymerized chains with strong (covalent) intrachain bonds, weaker interchain interactions and moderate crosslinking may show entropic elasticity.[9] These glasses can self-organise into oriented structures by application of uniaxial stress, and then return to their original configurations when the stress is removed.

As the indentation measurements show that the glass containing 20% of B_2O_3 behaves differently when indented in different directions, we suggest for future works further investigation of the mechanical properties of this composition. Further investigation is recommended to check if the peculiar fracture pattern is an indicator of anisotropy or caused by other factors, for instance, an indication that the samples may not have been sufficiently flat or not properly annealed. Thus, it is recommended to repeat the nanoindentation test for this sample.

4. Conclusions and applications

The large and varied range of properties of the glasses developed in this work prove that the development of compositions with designed properties transforms glass into a versatile material, able to accommodate many different demands. In most of these compositions, P_2O_5 is the main compound, the glass former. The addition of other components, such as aluminium oxide, boron oxide, or other oxides originated from by-products, produce glasses with a higher O/P ratio. Investigations of the short- and intermediate-range structure of the glasses were not performed; however, they are encouraged, primarily in order to support a better understanding of the mechanical and optical properties.

All the produced samples have a low T_g in relation to a soda-lime or a borosilicate glass. The drastic reduction of the melting temperature allows for a more energy-saving manufacturing process. Along with the incorporation of by-products, it contributes to addressing the current appeal for a more sustainable glass manufacturing process. Combined with a high thermal stability and a coefficient of thermal expansion comparable or lower than the standard glasses, these compositions could be candidates for applications in building engineering.

Although advantageous from a perspective of saving emissions and energy, the addition of by-products to the glass can be problematic as it introduces to the batch many components usually avoided by glass manufacturers, such as iron oxide. An alternative to avoid the contamination of furnaces, is to melt the glasses excluding the components present in the lowest concentrations, as it is assumed that they do not add beneficial properties to the material. For instance, eliminating all the components present in concentrations lower than 1 mol%, the Fe_2O_3 would be eliminated from the sample $70KPO_3$–$15FA$–$15Al_2O_3$. It brings a possibility to produce colorless glasses, and simplifying the composition to a formula containing only SiO_2, Al_2O_3, K_2O, CaO and P_2O_5. We encourage the reproduction of the samples using pure reagents instead of fly ash, and, therefore, eliminating the impurities present in the by-products, as well as a comparison of the properties of these glasses with the ones produced with the incorporation of fly ash.

The combination of low glass transition temperatures, high thermal stability and low thermal expansion, along with the production of samples based on the nominal composition, excluding impurities and using high purity reagents, eliminates variations in composition caused by the use of fly ash and could produce samples used for more advanced technologies. For instance, these glasses are candidates to be 3D printed, mainly sample $40KPO_3$–$25FA$–$15Al_2O_3$–$20B_2O_3$, with the lowest coefficient of thermal expansion. This promising process has distinct advantages over traditional methods of fabrication. Notably, the fact that 3D printing is capable of producing complex shapes that other manufacturing methods cannot handle, allowing the production of components such as glass connectors. 3D printing can design and print components with variable thicknesses and complex inner features, unlike glass blowing, where the inner features reflect the outer shape.[32] However, glass is inherently a very difficult material to work with. It requires a high temperature system, above 1000°C, and the viscosity changes significantly with temperature, requiring precise control of the temperature at all stages of the process.[32] The high melting temperature of glasses as fused silica combined with a high thermal expansion, that can lead to cracking, are drawbacks that have made standard glass compositions unreachable to three-dimensional printing.

High expansion glasses with good chemical durability are desirable for applications such as bonding with plastics or metals, since the thermal expansion coefficient of the joining materials should be very similar. Some of the developed samples could be used for this purpose, as they have a CTE very similar to a 446 stainless steel, which possess a CTE of about $11·4×10^{-6}$/°C.[33] However, samples with concentrations of KPO_3 higher than 70 mol% should not be designed to applications that require a high water resistance.

There is no absolute measure of chemical durability and glass types are generally graded relative to one another after subjecting them to similar experimental conditions, i.e. the nature of the experiment usually determines the relative order or durability. On the one hand, accelerated tests can be performed in a controlled environment, however, the validity of the experiment can be compromised by not reflecting real-life conditions. On the other hand, long-term tests can be conducted, however, these present a challenge to continuity and experimental logistics. Long-term tests are generally conducted under a less controlled environment and are more representative of real conditions. Other test conditions can also change: the protocols (static or dynamic) and the sample preparation can be altered, while the glass itself can be tested as a whole article or as a powder. In our work, samples were tested statically. The samples were tested under demineralised water and ambient temperature (around 20°C) in plastic vessels. These glass types demonstrated high water resistance in relation to general phosphate glass types. As an example, the reported compositions $54·5P_2O_5$–$20·5K_2O$–$20·5Cs_2O$–$4·5Al_2O_3$ and $50P_2O_5$–$16·7Na_2O$–$16·7K_2O$–$16·7Cs_2O$ had a mass loss of 19·3% and 100%, respectively, when dipped in water at 18°C for 1 h,[34] while the glasses reported in this work were kept in similar conditions for 30 days without any mass loss. Finding a concentration of P_2O_5 low enough to produce a durable material but high enough to keep the high expansion, such as sample $60KPO_3$–$30FA$–$10Al_2O_3$, is key for applications such as glass-to-metal seals.

Acknowledgements

References

1. Hoornweg, D., Bhada-Tata, P. & Kenney, C. A. Peak waste: when is it likely to occur? *J. Ind. Ecol.*, 2015, **19**, 117–28.
2. *Production and use of coal combustion products in the U.S. Market forecast through 2033*. American Road & Transportation builders association. 2015. Available at: https://www.acaa-usa.org/Portals/9/Files/PDFs/ReferenceLibrary/ARTBA-final-forecast.compressed.pdf (accessed on 23 Jan 2020).
3. Adams, T. H. *Fly ash use in concrete increases slightly as overall coal ash recycling rate declines*. American Coal Ash Association. 2020. Available at: https://www.acaa-usa.org/Portals/9/Files/PDFs/Coal-Ash-Production-and-Use.pdf (accessed on 23 Jan 2020).
4. *World Energy Outlook 2019*. ISBN 978-92-64-97300-8. 2019.
5. Rastogi, A. & Paul, V. K. A critical review of the potential for fly ash utilisation in construction-specific applications in India. *J. Environ.*

Res. Eng. Manage., 2020, **76** (2), 65–75.

6. Adams, T. H. Ash at Work: Applications, Science, and Sustainability of Coal Ash. American Coal Ash Association (ACAA), 2018, Issue I.

7. Zschimmer, E. *Chemical Technology of Glass*. Society of Glass Technology, Sheffield, 2013.

8. de Lima, C. L. J., Pastena, B., Nardi, R. P. R. D., Gouvea, Jnr., J. T., Ferrari, J. L., Cassanjes, F.C. & Poirier, G. Thermal, structural and crystallisation study of niobium potassium phosphate glasses. Mater. Res., 2015, 13–16.

9. Inaba, S., Hosono, H. & Ito, S. Entropic shrinkage of an oxide glass. *Nature Mater.*, 2015, **14**, 312–17.

10. de Lima, C. J., Veer, F., Çopuroglu, O. & Nijsse, R. Innovative glass recipes containing industrial waste materials. *Challenging Glass Conf. Proc.*, 2018, **6**, 533–42.

11. Hruby, A. Evaluation of glass-forming tendency by means of DTA. *Czech. J. Phys. B*, 1972, **22**, 1187–93.

12. Babadzhanova, O. F. & Yashchishin, I. N. Low-melting glasses based on phosphate ore processing products. *Glass Ceram.*, 2000, **57** (5), 3–5.

13. ElBatal, F. H., Hamdy, Y. M. & Marzouk, S. Y. UV-visible and infrared absorption spectra of transition metals-doped lead phosphate glasses and the effect of gamma irradiation. *J. Non-Cryst. Solids*, 2009, **355**, 2439–47.

14. Möncke, D., Papageorgiou, M., Winterstein-Beckmann, A. & Zacharias, N. Roman glasses coloured by dissolved transition metal ions: redox-reactions, optical spectroscopy and ligand field theory. *J. Archaeol. Sci.*, 2014, **46**, 23–36.

15. Minamf, T. & Mackenzie, J. D. Thermal expansion and chemical durability of phosphate glasses. *J Am Ceram. Soc.*, 1977, **60**, 232–5.

16. Sebastiani, M., Johanns, K. E., Herbert, E. G. & Pharr, G. M. Measurement of fracture toughness by nanoindentation methods: recent advances and future challenges. *Curr. Op Solid State Mater. Sci.*, 2015, **19**, 324–33.

17. Oyen, M. L. & Cook, R. F. A practical guide for analysis of nanoindentation data. *J. Mech. Behav. Biomed. Mater.*, 2009, **2**, 396–407.

18. Guo, H., Jiang, C. B., Yang, B. J. & Wang, J. Q. On the fracture toughness of bulk metallic glasses under Berkovich nanoindentation. *J. Non-Cryst. Solids*, 2018, **481**, 321–8.

19. Vella, J. B., Adhihetty, I. B., Junker, K., Volinsky, A. A. Mechanical properties and fracture toughness of organo-silicate glass (OSG) low-k dielectric thin films for microelectronic applications. *Int. J. Fracture*, 2003, **120**, 487–99.

20. Evans, A. G. & Charles, E. A. Fracture toughness determination by indentation. *J. Am. Ceram. Soc.*, 1976, **59**, 1976, 371–2.

21. Lawn, B. R., Evans, A. G. & Marshall, D. B. Elastic/plastic indentation damage in ceramics: the median/radial crack system. *J. Am. Ceram. Soc.*, 1980, **63**, 574–81.

22. Chen, J. & Bull, S. J. Assessment of the toughness of thin coatings using nanoindentation under displacement control. *Thin Solid Films*, 2006, **494**, 1–7.

23. Chen, J. Indentation-based methods to assess fracture toughness for thin coatings. *J. Phys. D*, 2013, 45, 1–15.

24. Laugier, M. T. Palmqvist indentation toughness in Wc–Co composites. *J. Mater. Sci. Lett.*, 1987, **6**, 897–900.

25. Niihara, K., Morena, R. & Hasselman, D. P. H. Evaluation of K_{Ic} of brittle solids by the indentation method with low crack-to-indent ratios. *J. Mater. Sci. Lett.*, 1982, **1**, 13–16.

26. Jang, J., Wen, S., Lance, M. J., Anderson, I. M. & Pharr, G. M. Cracking and phase transformation in silicon during nanoindentation. *MRS Proc.*, 2004, **795**, 313–18.

27. Scholz, T., Schneider, G. A., Munoz-Saldana, J. & Swain, M. V. Fracture toughness from submicron derived indentation cracks. *Appl. Phys. Lett.*, 2004, **84** (16), 3055–7.

28. Volinsky, A. A., Vella, J. B. & Gerberich, W. W. Fracture toughness, adhesion and mechanical properties of low-K dielectric thin films measured by nanoindentation. *Thin Solid Films*, 2003, **429**, 201–10.

29. Schiffmann, K. I. Determination of fracture toughness of bulk materials and thin films by nanoindentation: comparison of different models. *Philos. Mag.*, 2011, **91** (7–9), 1163–78.

30. Li, X., Diao, D., Bhushan, B. Fracture mechanisms of thin amorphous carbon films in nanoindentation. *Acta Mater.*, 1997, **45** (11), 4453–61.

31. Endo, J., Inaba, S. & Ito, S. Mechanical properties of anisotropic glass. *J. Am. Ceram. Soc.*, 2015, **98**, 2767–71.

32. Bradley, D. 3D printing transparent glass. *Mater. Today*, 2015, **18** (10), 531–2.

33. Brow, R. K. & Watkins, R. D. *High Expansion, Lithium Corrosion Resistant Sealing Glasses. United States Patent, 1991.*

34. *Inaba*, S. *Anisotropic glass.* United States patent application publication. 2016. Pub. No.: US 2016/0362328A1.